The Astrophysical Journal, 682:1363–1369, 2008 August 1

TRANSITION REGION VELOCITY OSCILLATIONS OBSERVED BY EUNIS-06

D. B. Jess
Astrophysics Research Centre, School of Mathematics and Physics, Queen's University, Belfast BT7 1NN, Northern Ireland, UK; and NASA Goddard Space Flight Center, Solar Physics Laboratory, Code 671, Greenbelt, MD 20771; djess01@qub.ac.uk

D. M. Rabin and R. J. Thomas
NASA Goddard Space Flight Center, Solar Physics Laboratory, Code 671, Greenbelt, MD 20771

J. W. Brosius
Catholic University of America at NASA Goddard Space Flight Center, Solar Physics Laboratory, Code 671, Greenbelt, MD 20771

and

M. Mathioudakis and F. P. Keenan
Astrophysics Research Centre, School of Mathematics and Physics, Queen's University, Belfast BT7 1NN, Northern Ireland, UK
Received 2008 January 23; accepted 2008 April 9

ABSTRACT

Spectroscopic measurements of NOAA AR 10871, obtained with the Extreme Ultraviolet Normal Incidence Spectrograph (EUNIS) sounding rocket instrument on 2006 April 12, reveal velocity oscillations in the He II 303.8 Å emission line formed at $T \approx 5 \times 10^4$ K. The oscillations appear to arise in a bright active region loop arcade about 25″ wide which crosses the EUNIS slit. The period of these transition region oscillations is 26 ± 4 s, coupled with a velocity amplitude of ± 10 km s^{-1}, detected over four complete cycles. Similar oscillations are observed in lines formed at temperatures up to $T \approx 4 \times 10^5$ K, but we find no evidence for the coupling of these velocity oscillations with corresponding phenomena in the corona. We interpret the detected oscillations as originating from an almost purely adiabatic plasma, and infer that they are generated by the resonant transmission of MHD waves through the lower active region atmospheres. Through the use of seismological techniques, we establish that the observed velocity oscillations display wave properties most characteristic of fast body global sausage modes.

Subject headings: Sun: activity — Sun: oscillations — Sun: transition region — Sun: UV radiation

Online material: color figures

1. INTRODUCTION

The discovery of solar oscillations in the 1960s (Leighton 1960) and the identification of individual wave modes enabled accurate information on the properties of the solar interior to be established. These discoveries thereafter developed into the prominent research area of helioseismology (Pomerantz et al. 1985; Duvall & Harvey 1984; Scherrer et al. 1982). The discovery of oscillations in coronal structures raised the prospect of using these oscillations as a diagnostic tool to establish coronal loop parameters. The field of coronal seismology subsequently emerged (Roberts 2000; Aschwanden et al. 2004; Nakariakov et al. 2004; Ofman 2007). The identification of waves with wavelengths shorter than the size of typical coronal structures imposes great demands on current spectroscopic and imaging instruments. The contribution of high-frequency waves to the heating of coronal structures may be significant (Porter et al. 1994). However, current space-borne instruments lack the necessary spatial, spectral, and temporal resolution required to probe such small-scale structures. Extensive analyses of photospheric oscillations have shown evidence for high-frequency, reconnection-driven acoustic wave trains (Jess et al. 2007b). High-cadence observations of the upper solar atmosphere are much more scarce, primarily due to telemetry restrictions imposed by space-borne experiments. One such study was carried out by Williams et al. (2001), who detected a 6 s intensity oscillation associated with an active region coronal loop. This oscillation was subsequently interpreted as a fast-mode, impulsively generated, magnetoacoustic wave (Williams et al. 2002).

The transition region, with a very dynamic nature over an inherently small depth, provides a regime to fully explore the potential coupling of underlying wave trains to those found in the corona (Doschek 2006). Recent work by Gömöry et al. (2006) discusses the detection of transition region velocity oscillations with periodicities in the range 250–450 s and proposes this as evidence of downward-propagating waves. Doyle et al. (1998) found transition region intensity oscillations with periods ranging from 200 to 500 s, while Hansteen et al. (2000) report both intensity and velocity oscillations in the transition region with periods ranging from 100 to 300 s. In addition, De Pontieu et al. (2005) find, through the use of numerical models, that oscillations generated in the photosphere can propagate into the corona, provided they are guided along an inclined magnetic flux tube. Although there have been many detections of transition region oscillations, space-borne instrumentation lacks the temporal resolution required to probe waves with frequencies above 33 mHz in this part of the solar atmosphere. The reason for this may be the lack of instruments available which are sensitive enough to obtain good count statistics, while maintaining short exposure times necessary for high-cadence observations. In order to probe physical processes occurring in the transition region on timescales of less than 1 minute, it is imperative to acquire data at the highest possible cadence using a sensitive camera system.

Here we report velocity oscillations detected in the transition region using an Extreme Ultraviolet Normal Incidence Spectrograph (EUNIS) sounding rocket instrument developed at NASA's Goddard Space Flight Center. In § 2 we provide a brief outline of the observations, while in § 3 we discuss the methodologies

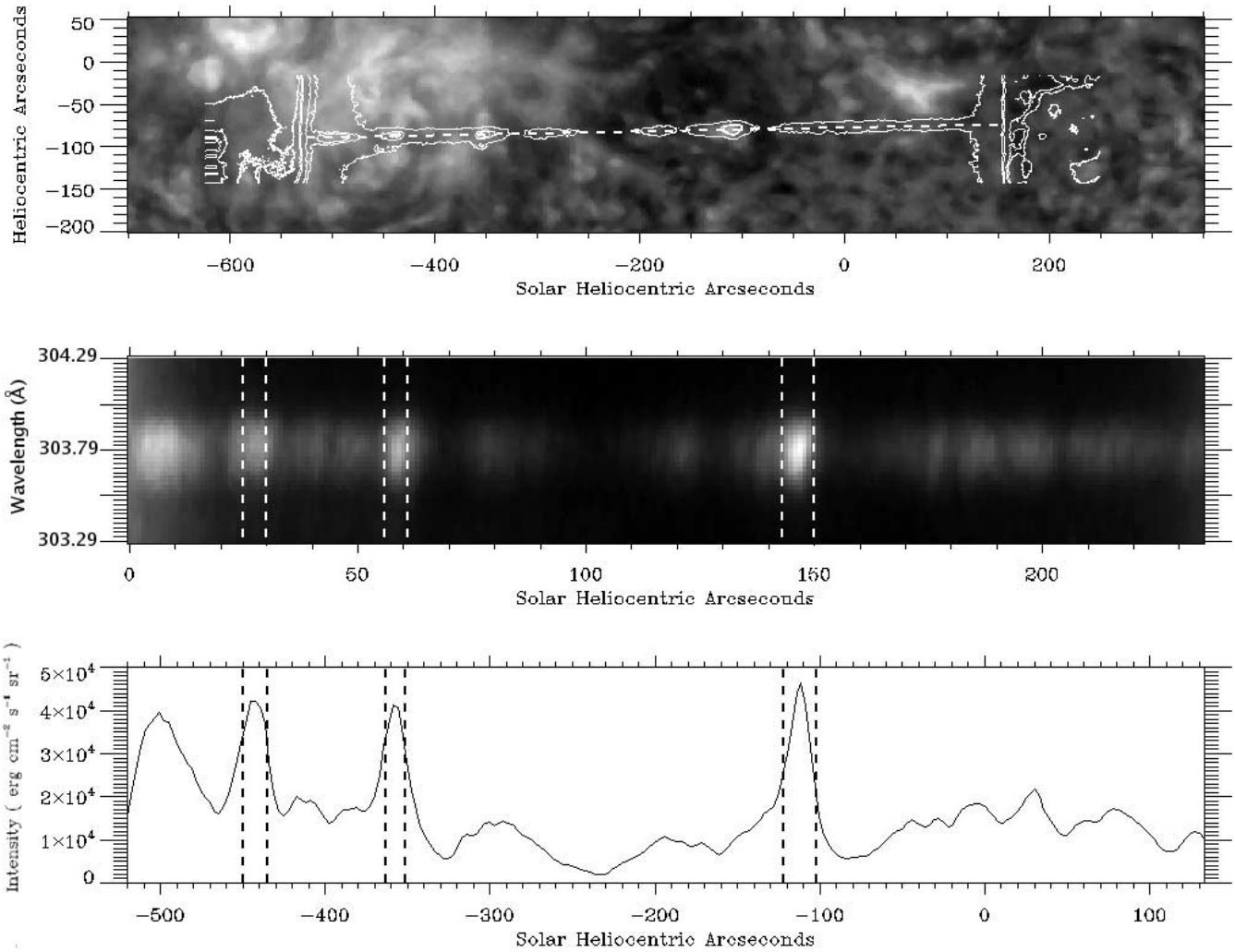

FIG. 1.— *Top*: EUNIS LW slit position, at the start of the stare sequence, after co-alignment with EIT's 304 Å image. *Middle*: Snapshot of the LW detector, cropped to only include contributions from the He II emission line, as a function of position along the slit. *Bottom*: Integrated He II intensity as a function of position along the slit. Both the middle and bottom panels are overplotted with vertical dashed lines, indicating the boundaries of three bright transition region features, outlined in § 3. Velocity oscillations were detected in Feature 2.

used during the analysis of the data and the search for reliable oscillatory signatures. A discussion of our results in the context of velocity oscillations is in § 4, and finally, our concluding remarks are given in § 5.

2. OBSERVATIONS

EUNIS was launched from White Sands Missile Range, New Mexico, at 1810 UT on 2006 April 12. It achieved a maximum altitude of 313 km and obtained solar spectra and images between 1812 and 1818 UT. EUNIS observed NOAA AR 10871 (S07°, E28°) and AR 10870 (S08°, W02°), the quiet area between them, and a southern hemisphere coronal bright point within the quiet area. For the present study, we are concerned with 75 solar exposures taken during a "stare" (fixed pointing) mode near the start of the flight, with constant 1.024 s durations. Each of the data frames consists of imaged extreme-ultraviolet (EUV) spectra along a slit 660″ long, together with spectroheliograms (called lobe images) formed by 200″ wide areas beyond the two slit ends, which are used for spatial registration. For this analysis, we will focus on the long-wave (LW) channel, where the spectral coverage ranges from 300 to 370 Å, with an associated cadence of ≈2 s. Further observations in scanning (spectroheliogram) mode are not discussed here. Additional details regarding the EUNIS instrument can be found in Brosius et al. (2007).

3. DATA ANALYSIS

Processing the EUNIS images was performed by subtracting an average dark frame obtained in flight, debiasing each detector row with a linear fit to the unilluminated ends, correcting for nonlinear detector response, and applying a flat-field image obtained in the laboratory after the flight. Radiometric calibration, carried out postflight at Rutherford Appleton Laboratory, and corrections for atmospheric extinction, are also included. Brosius et al. (2008) discuss validation of the EUNIS relative and absolute radiometric calibration.

Comparison of EUNIS He II 303.8 Å lobe images with a full-Sun He II image obtained at 1812 UT with *SOHO*'s EUV Imaging Telescope (EIT) reveals that the EUNIS LW slit was tilted about 1.5° counterclockwise from the solar east-west axis, and that this angle remained stable in time. The EUNIS LW field of view was initially centered at ($x = -193''$, $y = -83''$), but its pointing drifted at a steady rate of about 0.06 arcsec s^{-1} in both the x- and y-directions, which corresponds to a net drift in each dimension of about 10″ during the 167 s spent in this mode. Due to the drift

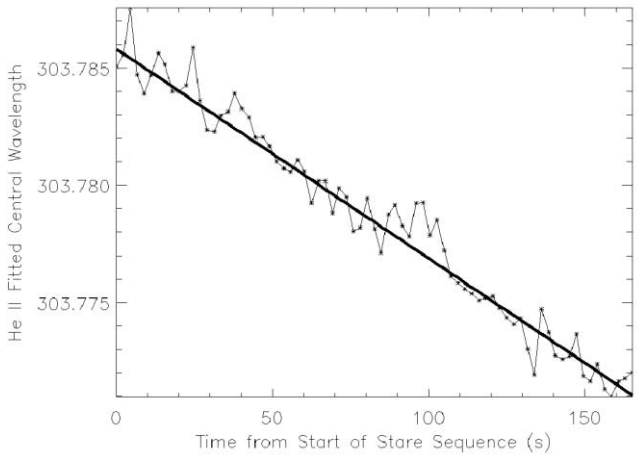

FIG. 2.—Slit-averaged wavelength (*stars*) for each of the 75 one-second stare exposures, plotted as a function of time from the start of the stare sequence. For each exposure, the slit-averaged wavelength was derived by taking the average of the fitted centroid wavelength for each spatial pixel along the slit, as outlined in § 3. Note the decrease in apparent wavelength with time, believed to be caused by thermal effects within the EUNIS payload. Overplotted on the diagram, using a solid, bold line, is a least-squares linear fit to the data, which is used to remove this systematic wavelength shift.

in the solar *x*-direction being along the slit axis, we were able to remove this spatial shift through co-alignment techniques. Implementing Fourier cross-correlation routines as well as squared mean absolute deviations, we were able to provide subpixel co-alignment accuracy. However, it must be noted that subpixel image shifting was not implemented due to the substantial interpolation errors which may accompany this technique. Drift of the EUNIS LW field of view in the solar *y*-direction was not compensated for, since the overall drift is greater than the $\approx 2''$ slit width.

After co-alignment of the EUNIS LW spectra, we averaged over three spatial pixels for a net spatial pixel size of $2.8''$. Line fits were then made using Gaussian profiles on linear backgrounds, resulting in values of the centroid position, integrated intensity, and FWHM, together with their corresponding uncertainties, at each spatial location along the slit and for each EUNIS exposure. Figure 1 shows the pointing of the EUNIS LW slit near the beginning of stare sequence, along with the simultaneous He II slit image and corresponding line intensity as a function of position along the slit. NOAA AR 10871, which is the subject of this paper, is located toward the left-hand side of Figure 1. The EUNIS spectral resolution for this first flight was $\approx$200 mÅ FWHM in the LW channel; still, the centroids of strong lines, such as with He II reported here, can be determined with a statistical uncertainty of ± 2 km s^{-1} or better (Brosius et al. 2007).

Since EUNIS does not provide an absolute wavelength scale, velocities reported here are relative to average values measured across individual solar features. For example, Figure 2 shows the slit-averaged He II central wavelength as a function of time from the start of the EUNIS stare sequence, and reveals a systematic shift toward shorter wavelength. The wavelength drift is modest, less than 1 pixel over the whole flight, but real. Its characteristics are identical in all observed LW lines, and does not depend on the solar feature being observed. These facts, coupled with the shape of the drift with time, suggest it is due to thermal changes within the payload, resulting in a tilt of the grating within its dispersion plane. To remove this effect, a least-squares linear fit is performed, after which the resulting trend is removed from the data, leaving pure deviations relative to the average value measured across the solar feature. Portions of the He II slit image were analyzed based on their relative magnitudes. Figure 1 shows the isolation of three distinct and intense features corresponding to a coronal bright point and two enhancements in NOAA AR 10871.

Relative He II velocities as a function of time are generated for each of the three features shown in Figure 1. Since the spatial averaging of three pixels has already been performed to improve the signal-to-noise ratio, no additional averaging was required. Thus, spatially resolved velocities are determined for each solar feature, allowing for more precise diagnostics. Before temporal analysis of the data set can be implemented, timing corrections must be considered. During the stare mode investigated here, all exposure durations were exactly the same, namely 1.024 s. However, time intervals between a small number of exposures varied somewhat. To compensate for this timing irregularity, all line-fit parameters were interpolated onto a constant-cadence time series with linear interpolation performed between data points. During this interpolation procedure approximately 15% of all data points required a timing correction. This provides the necessary platform for temporal studies to commence.

All spatially resolved He II velocity measurements were passed into fast Fourier transform (FFT) and wavelet analysis routines. While a FFT searches for periodic signatures by decomposing the input signal into infinite length sinusoidal wave trains using a basic exponential function, wavelet analysis utilizes a time-localized oscillatory function continuous in both frequency and time (Bloomfield et al. 2004) and is therefore highly suited in the search for transient oscillations. The wavelet chosen for this study is known as a Morlet wavelet and is the modulation of a sinusoid by a Gaussian envelope (Torrence & Compo 1998). Strict criteria were implemented during wavelet analysis to ensure that oscillatory signatures correspond to real periodicities. The first is a test against spurious detections of power that may be due to Poisson noise, where the input time series is assumed to be normally distributed (consistent with photon noise) and following a χ^2 distribution with 2 degrees of freedom. A 99% confidence level is calculated by multiplying the power in the background spectrum by the values of χ^2, corresponding to the 99th percentile of the distribution (Torrence & Compo 1998; Mathioudakis et al. 2003).

The second criterion applied is a comparison of the input time series with a large number (1500) of randomized time series with an identical distribution of counts. The probability, p, of detecting nonperiodic power is calculated for the peak power at each time step by comparing the value of power found in the input time series with the number of times that the power transform of the randomized series produces a peak of equal or greater power. A percentage confidence is attributed to the peak power at every time step in the wavelet transform by $(1 - p) \times 100$, such that a high value of p implies that there is no periodic signal in the data, while a low value suggests that the detected periodicity is real (see Banerjee et al. 2001).

Our final wavelet criterion is the exclusion of oscillations which last, in duration, less than 1.41 cycles. This is consistent with the decorrelation time defined by Torrence & Compo (1998). One can distinguish between a spike in the data and a harmonious periodic component at the equivalent Fourier frequency by comparing the width of a peak in the wavelet power spectrum with the decorrelation time. From this, the oscillation lifetime at the period of each power maximum is defined as the interval of time from when the power supersedes 95% significance to when it subsequently dips below 95% significance (McAteer et al. 2004). The lifetime was then divided by the period to give a lifetime in terms of complete cycles (Ireland et al. 1999). Any oscillations which last for less than this minimum duration were discarded, as they may have simply been a spike in the time series.

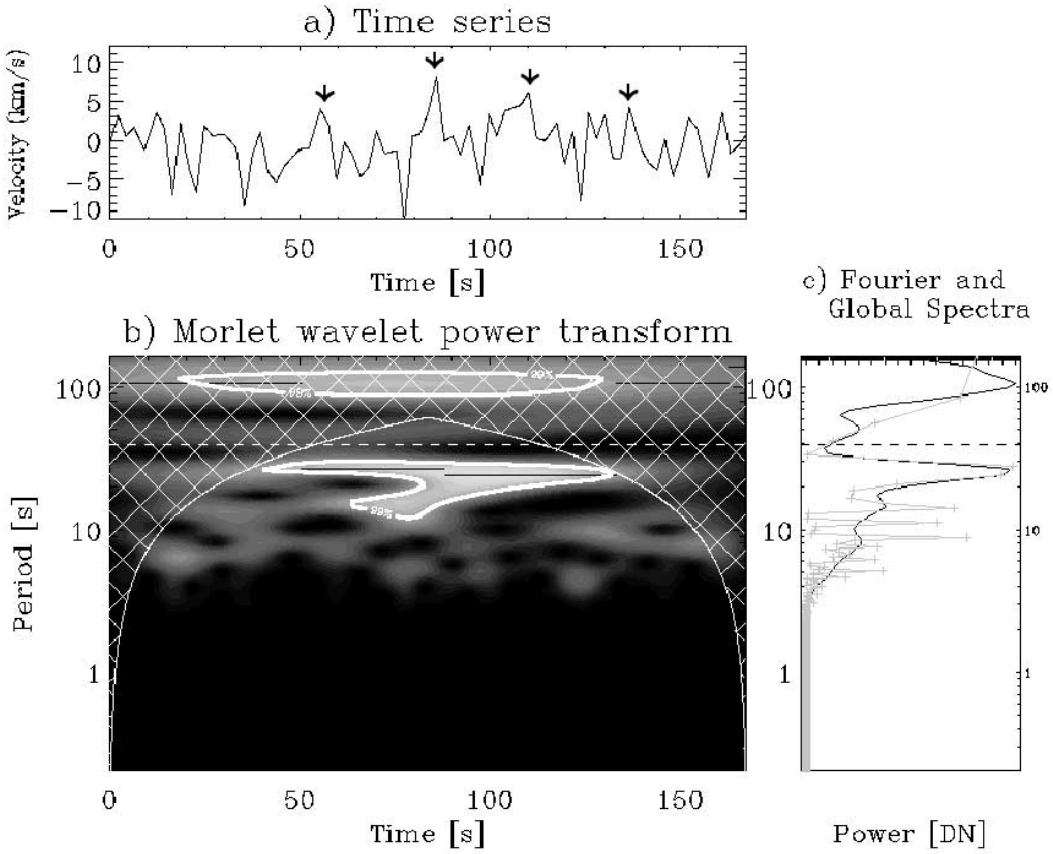

FIG. 3.— Wavelet diagram showing the detection of a 26 ± 4 s periodic velocity oscillation in He II, over four complete cycles, originating from Feature 2 (see Fig. 1). The original He II velocity time series is plotted in (*a*) with arrows indicating the peaks of the oscillation. The wavelet power transform, along with locations where detected power is at, or above, the 99% confidence level, are contained within the contours in (*b*). Plot (*c*) shows the summation of the wavelet power transform over time (*solid line*) and the fast Fourier power spectrum (*plus signs*) over time, plotted as a function of period. Both methods have detected a well-pronounced 26 s oscillation. The cone of influence (COI), the cross-hatched area in the plot, defines an area in the wavelet diagram where edge effects become important, and as such any frequencies inside the COI are disregarded. Periods above the horizontal line (*dashed*) fall within the COI. [*See the electronic edition of the Journal for a color version of this figure.*]

Wavelet power, for a variety of oscillatory periods which lay above the 95% significance level, was saved as the output of this analysis.

4. RESULTS AND DISCUSSION

In Figure 3 it is clear to see a strong 26 s oscillatory signal, coupled with an amplitude of ± 10 km s^{-1}, lasting in excess of four complete cycles. Through examination of the FWHM of corresponding Fourier and global spectra, in addition to the boundaries of the 99% confidence level contours, we can associate an error of ± 4 s to the detected periodic signal. This oscillatory frequency is much higher than previously detected and originates from the most westerly part of the active region (Feature 2). Similar analysis of the intensity variation of Feature 2 reveals no intensity oscillations at this location. Through closer examination of the EIT 304 Å image, the location of strong oscillatory power originates from a particularly bright part of NOAA AR 10871. Due to the EUNIS instrument providing spatially resolved spectra, pixels of the EUNIS slit corresponding to this bright feature (eight in total) were analyzed in full. Each pixel, corresponding to a spatial scale of 2.8″ (as outlined in § 3), provides high oscillatory power at a 26 s periodicity. Furthermore, no phase difference between neighboring pixels was found, indicating that this oscillatory phenomena is of substantial physical size (in excess of 20″). The fact that the signal remains coherent during pointing drifts perpendicular to the slit direction indicates a size of at least 6″ in that dimension as well. Additional transition region lines were also studied, consisting of the Mg VI 349.2 Å ($T \approx 4.0 \times 10^5$ K), Ne IV 358.7 Å ($T \approx 1.6 \times 10^5$ K), and Ne V 359.4 Å ($T \approx 3.2 \times 10^5$ K) emission lines. All of these emission lines corroborate the detection of the 26 s velocity oscillation in Feature 2. However, due to these lines being much weaker when compared to He II, the resulting reduction in signal-to-noise ratio means that the confidence levels associated with these detections are reduced. Nevertheless, a strong 26 s oscillatory signal over four complete cycles, with confidence levels exceeding 85% in each instance, is observed in transition region emission lines formed at temperatures up to 4×10^5 K.

Due to the full-disk nature of EIT and Michelson Doppler Imager (MDI) images, these can be accurately co-aligned by forcing the solar limbs to agree (López Fuentes et al. 2006). Through multiple co-alignments an uncertainty between EIT and MDI images converges to approximately 0.5 of an EIT pixel, or 1″. This is an intermediary step which allows subsequent co-alignment of *TRACE* images to MDI magnetograms. On inspection of a co-aligned *TRACE* 195 Å image, it is clear that the oscillatory phenomena is generated in the immediate vicinity of a coronal loop structure (Fig. 4). This, coupled with the strong underlying photospheric magnetic field (top panel of Fig. 4), suggests that this could be an observational signature of a propagating MHD wave. Highly magnetic structures, such as coronal loops, can act as superior waveguides (Edwin & Roberts 1983), which allow the

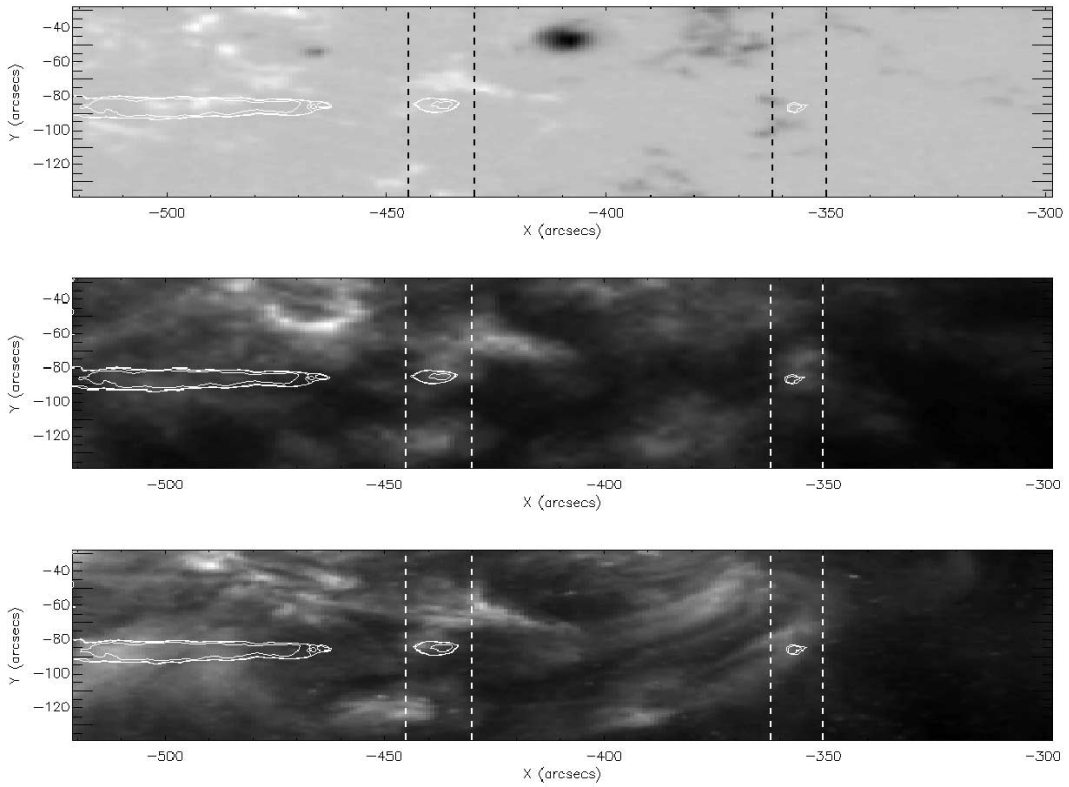

FIG. 4.—*Top*: MDI magnetogram; *middle*: EIT 304 Å transition region image; *bottom*: *TRACE* 195 Å coronal image. Each image was taken around the time of the EUNIS launch, and therefore acts as a good two-dimensional reference to compare with the one-dimensional, spectroscopic results of EUNIS. Overplotted in each diagram are vertical dashed lines, corresponding to the boundaries of Features 1 and 2 (§ 3 and Fig. 1), as well as He II intensity contours from the EUNIS LW slit. Note how Features 1 and 2 are located very close to regions of opposite magnetic polarity.

efficient propagation of MHD waves. To search for upward-propagating waves, we perform the same rigorous analysis on cospatial coronal emission lines. For this, we choose the strong Mg IX 368.1 Å ($T \approx 9.5 \times 10^5$ K), Fe XIV 334.2 Å ($T \approx 2.0 \times 10^6$ K), and Fe XVI 335.4/360.8 Å ($T \approx 2.5 \times 10^6$ K) emission lines. Due to structures at one level in the solar atmosphere not always overlying the structures to which they are connected at other levels in the atmosphere, we included additional EUNIS pixels during our search for coronal oscillations. Due to the EUNIS slit being one-dimensional, we are unable to investigate any oscillatory behavior at locations north and south of the EUNIS pointing. However, we analyze pixels lying to the east and west of the detected He II oscillations. We incorporate an extra 4 pixels in each direction into our investigation, totalling an additional 22.4″. After searching for simultaneous oscillations in these lines, no velocity perturbations could be found in the corona. In addition, no periodic signatures in coronal emission intensities could be found, implying that our detected transition region oscillations are not propagating out into the corona.

To check the validity, and reliability, of our detected He II velocity oscillation, we examine the results of analyzing two additional features mentioned in § 3. One feature corresponds to the central portion of NOAA AR 10871 (Feature 1), while the second coincides with the coronal bright point found to the west of the active region (Feature 3). Examining these two features in detail reveals no signatures of He II velocity oscillations. It is interesting to note that Feature 1 overlies a region of opposite magnetic polarity to that of Feature 2 (Fig. 4). In addition, the MDI magnetogram shows that the magnetic field is stronger for Feature 2 than for Feature 1. In accordance with the theory of Edwin & Roberts (1983), this may imply that the magnetic structuring around Feature 2 may act as a better waveguide than the magnetic field found surrounding Feature 1. In addition, the velocity fluctuations of the He II line are consistent with the relative Doppler velocities reported by Brosius et al. (2007).

Such a scenario leaves open the issue of what causes these transition region velocity oscillations. De Pontieu et al. (2003) state that there is a general correspondence between *p*-modes and upper transition region oscillations, in duration, periods, and locations of oscillatory power. Priest (1982) explains that the superposition of *p*-mode oscillations usually results in wave trains containing four or five cycles, after being emitted from the photosphere. This is corroborated by De Pontieu et al. (2003), who find transition region oscillations typically consisting of wave trains 3–7 cycles long. The cycle lifetimes stated by De Pontieu et al. (2003) and Priest (1982) match our findings closely; however, these pressure-driven modes cannot explain the velocity oscillations presented in this work. Traditionally, transition region velocity oscillations, surrounding an active region, have been interpreted as the signature of resonant transmission of chromospheric umbral oscillations (Thomas et al. 1987). Previously detected transition region velocity oscillations have associated periods of 129–173 s (Gurman et al. 1982) and directly corroborate the work of Thomas et al. (1987).

Since there are no low-temperature lines in the EUV bandpasses of EUNIS, it provides no direct information about chromospheric plasmas. Therefore, we are unable to provide a quantitative comparison to the work of Gurman et al. (1982), who detect transition region and chromospheric velocity oscillation interplay in highly magnetic structures. Nevertheless, the fact that we detect pure velocity oscillations, with no intensity variation, implies that we are dealing with an almost purely adiabatic plasma (Rendtel

et al. 2003). Models of coupled resonators (Žugžda et al. 1983, 1987; Settele et al. 1999), which explain the resonant transmission of MHD waves through active region atmospheres, require regions of strong wave reflection, e.g., from the steep temperature gradient found within the transition region. Consequently, according to Rendtel et al. (2003), velocity oscillations may be observed in the EUV lines of active regions as a result of resonant transmission. If intensity oscillations were found to accompany transition region velocity waves, this would hint at a nonadiabatic system consisting of isothermal waves (Staude et al. 1985). Such a distinction is important, as it indicates that the solar transition region plasma for Feature 2 is adiabatic in nature, and experiences strong, nonstationary behavior over the duration of the EUNIS stare mode. Therefore, through comparison of our results to those of Gurman et al. (1982), Rendtel et al. (2003), and Thomas et al. (1987), we can infer that our detected transition region velocity oscillations are similar in both amplitude and location to those found interacting with chromospheric plasma (Brynildsen et al. 1999). We find the oscillations propagating in a concentrated magnetic field region with much higher frequencies than reported to date.

Of particular importance is the ability to place the observed He II oscillation onto a dispersion diagram (Edwin & Roberts 1983). From this diagram, it is possible to infer the exact mode of propagation in relation to fast or slow body waves. Several kinds of wave modes have been directly observed with the *TRACE* and *SOHO* spacecraft, as well as with ground-based telescopes (Aschwanden et al. 1999; Wang et al. 2002). It is of particular interest that these wave modes, through use of MHD seismology techniques, can be deduced from simple plasma parameters such as electron density and magnetic field strength (Nakariakov et al. 1999; Nakariakov & Ofman 2001). One particular mode, the sausage mode, has been typically used to interpret short periodicities of less than 1 minute. The sausage mode is based on an assumption whereby the period of this mode is determined by the ratio of the cross-sectional radius to the Alfvén speed inside the waveguide (Meerson et al. 1978). The global sausage mode (GSM) is a fast MHD mode which can efficiently modulate the plasma density and magnetic field strength. It is also one of the principal modes that can be excited in active regions, provided the magnetic waveguide is sufficiently thick and dense. In order to assess whether the GSM can be supported in the transition region of NOAA AR 10871, we require information on the plasma temperature, electron density, and magnetic field strength.

For this assessment, we choose a plasma temperature of $T \approx 5 \times 10^4$ K (the formation temperature of He II), an internal waveguide electron density of $n_e^i \approx 10^{11.5}$ cm^{-3}, an external waveguide electron density of $n_e^e \approx 10^{10.7}$ cm^{-3}, and a magnetic field strength of 25 G. These values are consistent with previously measured transition region values (Parnell et al. 2002; Pérez et al. 1999). The GSM exists if the dimensionless wavenumber, $k\alpha$, is greater than the cutoff value,

$$k_c\alpha = j_0 \sqrt{\frac{(C_{S0}^2 + C_{A0}^2)(C_{Ae}^2 - C_{T0}^2)}{(C_{Ae}^2 - C_{A0}^2)(C_{Ae}^2 - C_{S0}^2)}}, \quad (1)$$

where α is the waveguide radius and $j_0 = 2.4$ is the first zero of the Bessel function $J_0(x)$, as detailed in Edwin & Roberts (1983); C_{A0} and C_{Ae} are the internal and external Alfvén speeds, while C_{S0} and $C_{T0} = C_{S0}C_{A0}/(C_{S0}^2 + C_{A0}^2)^{1/2}$ are the internal sound and tube speeds, respectively. These values can be derived directly from our input parameters described above, and following the criteria outlined in Nakariakov et al. (2003), we can determine if this mode can explain the oscillations presented here. We derive the associated cutoff value, $k_c\alpha$, to be 1.12. In order to see whether the observed wave train is a fast or slow body wave, we relate the detected periodicity, P, to the internal Alfvén speed, whereby a fast body wave will be present if

$$\alpha > \frac{j_0 C_{A0} P}{2\pi}. \quad (2)$$

Substituting known values into equation (2), we find that the minimum diameter of the waveguide required to channel fast body waves is ≈1800 km. We can use cospatial coronal observations to provide an estimate of the diameter of the transition region waveguide. By measuring the cospatial width of coronal loops seen in the *TRACE* 195 Å images, we establish an average loop width of 7 *TRACE* pixels, corresponding to a diameter of ≈2500 km. This measured width is consistent with previous *TRACE* statistical loop measurements (Aschwanden et al. 2000; Aschwanden & Nightingale 2005) and is greater than the minimum diameter required to channel fast body waves. Accompanying our derived $k_c\alpha$ value, we deem that a fast MHD wave (i.e., the GSM) could explain the origins of the detected He II velocity oscillation (Fig. 5). In addition to He II, the warmer transition region lines for which periodic velocity oscillations were detected are also consistent with the GSM. Increasing the line formation temperature from 5×10^4 to 4.0×10^5 K leads to an increase in the sound and tube speeds, whereas the internal and external Alfvén speeds remain unchanged. As a result, the cutoff value is increased, thus maintaining the validity of the GSM as the most favorable mode of propagation.

However, it must be noted that the cutoff value, $k_c\alpha$, is extremely sensitive to the assumed values of magnetic field strength

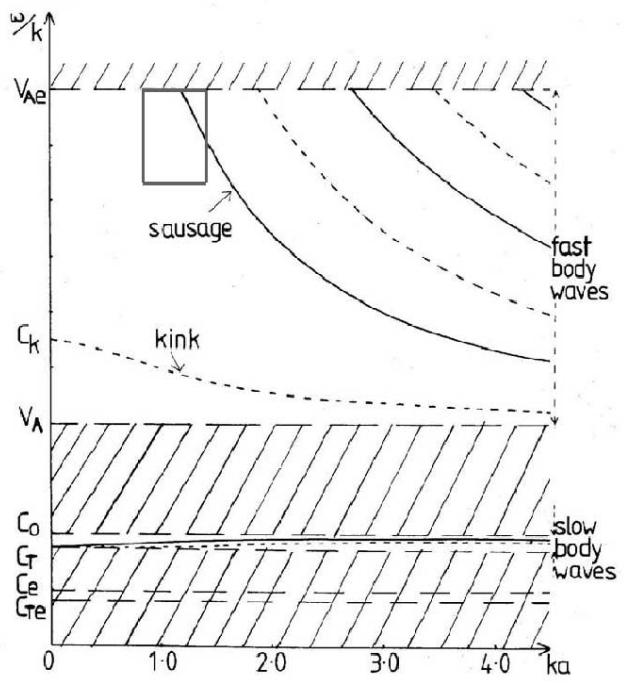

FIG. 5.—Phase speed ω/k, shown for magnetoacoustic waves in a cylindrical waveguide (with radius α) as a function of the dimensionless longitudinal wavenumber $k\alpha$ under the transition region/coronal conditions $C_{Ae} > C_{A0} > C_{T0} > C_{S0}$. Solid lines show the sausage modes, while the dashed lines indicate kink modes (Edwin & Roberts 1983). The solid box indicates the region on the dispersion curve in which the observed He II velocity oscillations lie. [*See the electronic edition of the Journal for a color version of this figure.*]

and electron density, through their relationship with the Alfvén speed, C_A. Furthermore, the magnetic field strength is almost always an inferred measure (Parnell et al. 2002) and exerts a stronger variation on the Alfvén speed due to a linear dependence between them. Therefore, caution must be exercised when evaluating the mode of propagation. In this instance, the GSM appears to be the most favorable mode of propagation, although for a definitive answer, values of magnetic field strength and electron density must first be determined accurately.

5. CONCLUDING REMARKS

We have presented direct evidence of high-frequency waves propagating in an active region, at transition region heights. We have shown the location of 26 s oscillatory signatures, with significance levels greater than 95% due to the rigorous wavelet criteria enforced in § 3. The velocity oscillations detected here originate from a large (>20″), bright He II structure crossing the EUNIS slit on the westerly edge of NOAA AR 10871. The highest temperature at which we observe this oscillation is 4×10^5 K, but we find no evidence for upward propagation of this wave train into the corona, and infer, qualitatively, that the detected oscillations could be caused by the resonant transmission interplay between the chromosphere and transition region. We deduce that the observed velocity oscillations exhibit signatures of a fast MHD wave—in particular, that of the fast body global sausage wave mode. The work of De Pontieu et al. (2003) emphasizes the coupling of transition region oscillations to those in the underlying photosphere. A natural extension of this work is to investigate if such a correspondence also exists in the high-frequency domain (see Jess et al. [2007a] for high-frequency photospheric analysis).

D. B. J. is supported by a Northern Ireland Department for Employment and Learning studentship. D. B. J. additionally thanks the NASA Goddard Space Flight Center for a CAST studentship—in particular Doug Rabin, Roger Thomas, and Jeff Brosius deserve special thanks for their endless help, support, and scientific input. F. P. K. is grateful to AWE Aldermaston for the award of a William Penney Fellowship. The EUNIS program is supported by the NASA Heliophysics Division through its Low Cost Access to Space Program in Solar and Heliospheric Physics. We thank the entire EUNIS team for the concerted effort that led to a successful flight. Wavelet software was provided by C. Torrence and G. P. Compo.[1]

[1] Wavelet software is available at http://paos.colorado.edu/research/wavelets/.

REFERENCES

Aschwanden, M. J., Fletcher, L., Schrijver, C. J., & Alexander, D. 1999, ApJ, 520, 880
Aschwanden, M. J., Nakariakov, V. M., & Melnikov, V. F. 2004, ApJ, 600, 458
Aschwanden, M. J., & Nightingale, R. W. 2005, ApJ, 633, 499
Aschwanden, M. J., Nightingale, R. W., & Alexander, D. 2000, ApJ, 541, 1059
Banerjee, D., O'Shea, E., Doyle, J. G., & Goossens, M. 2001, A&A, 371, 1137
Bloomfield, D. S., McAteer, R. T. J., Mathioudakis, M., Williams, D. R., & Keenan, F. P. 2004, ApJ, 604, 936
Brosius, J. W., Rabin, D. M., & Thomas, R. J. 2007, ApJ, 656, L41
Brosius, J. W., Rabin, D. M., Thomas, R. J., & Landi, E. 2008, ApJ, 677, 781
Brynildsen, N., Kjeldseth-Moe, O., Maltbys, P., & Wilhelm, K. 1999, ApJ, 517, L159
De Pontieu, B., Erdélyi, R., & De Moortel, I. 2005, ApJ, 624, L61
De Pontieu, B., Erdélyi, R., & De Wijn, A. G. 2003, ApJ, 595, L63
Doschek, G. A. 2006, ApJ, 649, 515
Doyle, J. G., van den Oord, G. H. J., O'Shea, E., & Banerjee, D. 1998, Sol. Phys., 181, 51
Duvall, T. L., & Harvey, J. W. 1984, Nature, 310, 19
Edwin, P. M., & Roberts, B. 1983, Sol. Phys., 88, 179
Gömöry, P., Rybák, J., Kučera, A., Curdt, W., & Wöhl, H. 2006, A&A, 448, 1169
Gurman, J. B., Leibacher, J. W., Shine, R. A., Woodgate, B. E., & Henze, W. 1982, ApJ, 253, 939
Hansteen, V. H., Betta, R., & Carlsson, M. 2000, A&A, 360, 742
Ireland, J., Walsh, R. W., Harrison, R. A., & Priest, E. R. 1999, A&A, 347, 355
Jess, D. B., Andic, A., Mathioudakis, M., Bloomfield, D. S., & Keenan, F. P. 2007a, A&A, 473, 943
Jess, D. B., McAteer, R. T. J., Mathioudakis, M., Keenan, F. P., Andic, A., & Bloomfield, D. S. 2007b, A&A, 476, 971
Leighton, R. B. 1960, in IAU Symp. 12, Aerodynamic Phenomena in Stellar Atmospheres, ed. R. N. Thomas (Dordrecht: Kluwer), 321
López Fuentes, M. C., Klimchuk, J. A., & Démoulin, P. 2006, ApJ, 639, 459
Mathioudakis, M., Seiradakis, J. H., Williams, D. R., Avgoloupis, S., Bloomfield, D. S., & McAteer, R. T. J. 2003, A&A, 403, 1101
McAteer, R. T. J., Gallagher, P. T., Bloomfield, D. S., Williams, D. R., Mathioudakis, M., & Keenan, F. P. 2004, ApJ, 602, 436
Meerson, B. I., Sasorov, P. V., & Stepanov, A. V. 1978, Sol. Phys., 58, 165
Nakariakov, V. M., Arber, T. D., Ault, C. E., Katsiyannis, A. C., Williams, D. R., & Keenan, F. P. 2004, MNRAS, 349, 705
Nakariakov, V. M., Melnikov, V. F., & Reznikova, V. E. 2003, A&A, 412, L7
Nakariakov, V. M., & Ofman, L. 2001, A&A, 372, L53
Nakariakov, V. M., Ofman, L., DeLuca, E. E., Roberts, B., & Davila, J. M. 1999, Science, 285, 862
Ofman, L. 2007, ApJ, 655, 1134
Parnell, C. E., Bewsher, D., & Harrison, R. A. 2002, Sol. Phys., 206, 249
Pérez, M. E., Doyle, J. G., O'Shea, E., & Keenan, F. P. 1999, A&A, 351, 1139
Pomerantz, M. A., Fossat, E., Gelly, B., Grec, C., Harvey, J. W., & Duvall, T. L. 1985, Antarctic J. U. S., 20, 221
Porter, L. J., Klimchuk, J. A., & Sturrock, P. A. 1994, ApJ, 435, 482
Priest, E. R. 1982, Solar Magnetohydrodynamics (Dordrecht: Reidel)
Rendtel, J., Staude, J., & Curdt, W. 2003, A&A, 410, 315
Roberts, B. 2000, Sol. Phys., 193, 139
Scherrer, P. H., Wilcox, J. M., Christensen-Dalsgaard, J., & Gough, D. 1982, Nature, 297, 312
Settele, A., Zhugzhda, Y. D., & Staude, J. 1999, Astron. Nachr., 320, 147
Staude, J., Žugžda, Y. D., & Locāns, V. 1985, Sol. Phys., 95, 37
Thomas, J. H., Lites, B. W., Gurman, J. B., & Ladd, E. F. 1987, ApJ, 312, 457
Torrence, C., & Compo, G. P. 1998, Bull. Am. Meteor. Soc., 79, 61
Wang, T. J., Solanki, S. K., Curdt, W., Innes, D. E., & Dammasch, I. E. 2002, ApJ, 574, L101
Williams, D. R., et al. 2002, MNRAS, 336, 747
———. 2001, MNRAS, 326, 428
Žugžda, Y. D., Locāns, V., & Staude, J. 1983, Sol. Phys., 82, 369
———. 1987, Astron. Nachr., 308, 257